Low-cost CR-39 detectoralpha track automatic counting method based on YOLOv8 object detection model*

Hong-Bo Xu,[1] Yu-Xi Xie,[1] Feng Xiao,[1] Xin-Yue Yang,[1] Chen-Xi Zu,[1] Xian-Fa Mao,[1] Shi-Cheng Luo,[1] Jia Liu,[1] Cheng Luo,[1] Hao You,[1] Hao-Yu You,[1] Hong-Zhi Yuan,[1] and Yan-Liang Tan†

[1]*College of Physics and Electronic Engineering, Hengyang Normal University, Hunan Province 421001, China*

This study proposes a low-cost automated method for alpha track recognition and counting on CR-39 detectors, providing an effective tool for radon measurement based on CR-39 detectors. By integrating a microcontroller platform with the PY-QT library, a CR-39 image acquisition system was developed, capable of capturing a complete CR-39 detector into 527 images. An automatic recognition and counting model based on YOLOv8m was trained using a dataset of over 80000 alpha track samples. The model is capable of automatically identifying and counting alpha tracks in images. To evaluate the model's performance, 16 etched CR-39 detectors with varying alpha track densities were tested. These detectors were sourced from granite-related experiments or high radon concentration experiments, with alpha track counts ranging from several thousand to tens of thousands. The test results show that the percentage error of the counts provided by the YOLOv8m model remains within an ideal range, typically below 1%. Meanwhile, the track sizes on these detectors are primarily concentrated in the ranges of 12-22 μm (width) $\times$ 12-22 μm (length) and 30-40 μm (width) $\times$ 30-40 μm (length). Additionally, the study identifies the main factors affecting counting accuracy and proposes corresponding optimization solutions

Keywords: Radon, CR-39 detectors, Alpha track, YOLOv8m.

I. INTRODUCTION

Radon is a naturally occurring radioactive gas that is colorless and odorless, with a half-life of 3.82 days, and is widely present in the natural environment [1]. The radioactive progeny produced during its decay can be inhaled and deposited in the lungs and other organs, leading to internal exposure, which may cause cellular damage and even induce cancer. Research indicates that radon exposure is the second leading cause of lung cancer after smoking, and prolonged exposure to high concentrations of radon significantly increases the risk of lung cancer and may damage bronchial tissues [2], [3]. Therefore, accurately measuring radon concentrations in the environment not only helps assess public health risks but also provides a scientific basis for formulating effective protective measures, holding significant importance for safeguarding human health.

Currently, solid-state nuclear track detectors (SSNTDs) have been widely utilized in the nuclear field [4], [5]. Compared to electronic radon monitors such as RAD7, SSNTDs offer advantages including low cost, no need for power supply, and suitability for long-term monitoring, making them particularly ideal for multi-point deployment and field environments. They can be continuously exposed for several months, providing long-term average radon concentration data, while featuring compact size, portability, and no requirement for real-time operation. Additionally, SSNTDs exhibit strong resistance to environmental interference, enabling stable performance in complex conditions, and require no maintenance, further reducing operational costs and technical barriers. Polyallyl diglycol carbonate (CR-39 detectors) is a prominent example. The CR-39 detector exhibits high sensitivity to radon and other radioactive elements; When exposed to a radon-rich environment, the decay of radon generates radioactive particles that leave tracks on the CR-39 detector; After treating the CR-39 detector with corrosive solutions such as potassium hydroxide, these tracks are enlarged and become observable under an optical microscope [6–8]. By counting the alpha tracks on the CR-39 detector, along with the actual area of the detector and the measurement time, the radon concentration can be determined. In related research, CR-39 detectors have been utilized in various nuclear physics experiments and monitoring scenarios. For instance, in laser-induced deuterium-deuterium fusion reactions, CR-39 was employed to measure the primary yield of protons [9]. Additionally, CR-39 detectors were used to accurately measure the dose and analyze the beam characteristics of therapeutic carbon ion beams in water phantoms [10]. Furthermore, a radon monitor based on electrostatic collection and CR-39 detectors, which is less affected by humidity, was developed to simultaneously measure Rn-222 and Rn-220 [11]. These applications demonstrate the importance and versatility of CR-39 detectors in the fields of nuclear physics research and radiation monitoring.

However, radon measurement technology based on CR-39 detectors exhibits certain notable limitations at the counting level. The number of tracks on CR-39 detectors dynamically varies with changes in radon concentration and exposure time. Traditional track counting methods primarily rely on manual operations under a microscope, which are not only inefficient but also prone to causing visual fatigue for operators, particularly when the number of tracks is large and their density is high. Additionally, the manual adjustment process of the microscope may introduce displacement and vibrations, and these minor operational errors can significantly

* This work was supported by Postgraduate Scientific Research Innovation Project of Hunan Province (Grant No. CX20231259), Natural Science Foundation of Hunan Province (Grant No. 2023JJ50091), Project of Hunan Provincial Department of Education (Grant No. 23A0516)

† Corresponding author, Yan-Liang Tan, hytyl@163.com.

affect the accuracy of the counting results, thereby adversely impacting the reliability of radon concentration assessment. Numerous rapid measurement systems have been developed, such as the CR-39 automatic track measurement technology based on the Hamamatsu C-1285 multi-processor image analysis system [12], the automatic sliding scan system utilizing track shape analysis [13], the photometric method for measuring track density in Solid State Nuclear Track Detectors (SSNTDs) [14], and the precise measurement of alpha exposure on CR-39 detectors using UV-Vis spectrophotometry [15]. The development of these technologies has significantly improved measurement efficiency and accuracy, providing substantial convenience and strong support for radon measurement techniques based on CR-39 detectors. Currently, a variety of advanced products are available on the market, such as the Autoscan 60 developed by Thermo Electron Corporation (Santa Fe, MN, USA), the Radometer 2000 series introduced by Radosys Ltd. (Budapest, Hungary), the Taslimage system developed by Track Analysis Systems Ltd. (Bristol, U.K.), and the HSP-1000 manufactured by Seiko Precision (Chiba, Japan) [16]. These products exhibit distinct advantages in terms of performance parameters and functional characteristics, enabling them to meet diverse application scenarios and a wide range of user requirements. However, the instruments involved in these methods, as well as the products available on the market, remain relatively expensive.

It is worth noting that with the rapid advancement of artificial intelligence technology, the YOLO (You Only Look Once) series of object detection algorithms have been continuously iterated and updated, gradually becoming open-source [17]. The task of track counting on CR-39 detectors can essentially be regarded as a specialized object detection problem, involving the recognition and localization of track morphology. Therefore, the YOLO algorithm holds significant application potential in the field of track counting for CR-39 detectors. This algorithm divides the input image into multiple grids using a deep convolutional neural network, with each grid independently predicting the bounding box positions and class probabilities of targets, thereby achieving efficient and precise object detection. Currently, the YOLO algorithm has been widely applied. For instance, In the agricultural sector, numerous scholars have conducted in-depth research on the application of YOLO in disease detection. For instance, some studies have utilized the YOLO model to detect storage pests on the surface of grain piles [18]; others have accurately identified apple leaf diseases through the YOLO-Leaf method [19]; improved YOLO v5s models have been employed to detect external defects in potatoes [20]; the YOLO MSM algorithm has been used for rapid and precise detection of corn leaf diseases [21]; and the integration of YOLOv5m with multiple soft attention modules has enhanced the recognition of tomato leaf diseases [22]. In the automotive field, the adoption of the YOLO deep learning algorithm has improved the accuracy of 3D object detection for autonomous vehicles in complex environments [23]; additionally, integrating self-supervised learning with the YOLO v4 network has effectively addressed the issue of construction vehicle detection [24]. In the field of drones, the YOLO models have been utilized for object detection from thermal infrared images and videos captured by drones [25]; the enhanced YOLOv7-Tiny has been employed for object detection based on aerial images from drones [26]; and improved YOLO algorithms have been applied to detect formations during the flight of drone fleets [27]. In the sonar field, the CSC-YOLO algorithm has been utilized to detect shipwreck targets in side-scan sonar images [28]; a lightweight and efficient GCT-YOLOv5 target detection model has been developed for real-time target detection in side-scan sonar images [29]; and AGD-YOLO has further enhanced the accuracy of forward-looking sonar target detection by incorporating an attention-guided denoising convolutional neural network [30]. With continuous iterations and optimizations of the YOLO algorithm, its application scope will further expand, bringing intelligent solutions to more industries. The YOLO algorithm has been extensively applied and validated across multiple domains, and its exceptional performance further substantiates the feasibility of employing this algorithm for track counting tasks in CR-39 detectors.

This work develops a low-cost, efficient automated method based on YOLOv8m to read tracks on CR-39 detectors. Using hardware components such as a microcontroller, stepper motor, linear guide, microscope, and self-developed image acquisition software, the system is capable of performing image sampling of the entire CR-39 detector. A YOLOv8m model was trained using numerous track samples, which can be used to automatically detect and count tracks in the images, while also reconstructing the CR-39 detector images. Experimental tests were conducted on a total of 16 CR-39 detectors. The results demonstrated a high degree of consistency between the measured and corrected values across different confidence levels, and the coefficient of determination (R^2) from linear fitting was notably high, fully validating the reliability of the method. This approach can be effectively applied to track counting in radon measurement using CR-39 detectors, significantly enhancing the convenience and efficiency of CR-39-based radon measurement technology.

II. MATERIALS AND METHODS

A. Precision image acquisition system

Firstly, a computer-based image acquisition software was developed using the PY-QT framework. This software captures images from the CR-39 detector in real-time through a stereoscopic biological microscope (XSP-06) and an electronic eyepiece (MC-D200U(E)), displaying them on the software interface at a resolution of 1280×720, corresponding to an actual area of approximately 585.00μm × 329.00μm on the CR-39 detector. The XSP-06 stereoscopic biological microscope features high resolution and stable optical performance, enabling clear visualization of the sample's microstructure, while the MC-D200U(E) electronic eyepiece provides high-sensitivity image capture, ensuring the integrity and clarity of image details. The software functionalities include real-time image display, saving the currently

displayed image, and customizing the save path.

Secondly, a high-precision motion platform was constructed by integrating hardware components, including a microcontroller (STM32F103C8T6), a stepper motor driver module (A4988), a 42 stepper motor (17HS4401), a linear guide rail (equipped with a 1204 ball screw), and a 12V power supply. The platform employs the STM32F103C8T6 microcontroller as the core control unit. The A4988 stepper motor driver module ensures precise operation of the stepper motor through accurate current control and microstepping functionality. Additionally, the linear guide rail, designed with a 1204 ball screw, enhances the platform's positioning accuracy. The 12V power supply provides stable electrical support for the entire circuit. A newly designed stage was integrated into the platform, replacing the original microscope stage, with the schematic diagram and physical image of the overall structure are shown in Fig. 1. Based on current market prices, a rough estimate of the total cost for the aforementioned hardware equipment ranges approximately between 2000 and 4000 CNY. It should be noted that this estimate does not include the cost of computer equipment.

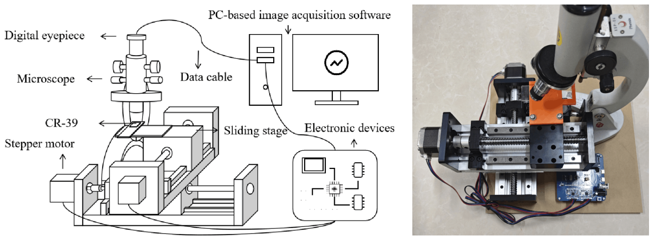

(a) (b)

Fig. 1. Structure diagram of the mobile platform: (a) schematic diagram of the structure, (b) physical prototype image.

The platform achieves bidirectional communication with the computer-based image acquisition software via a serial port. The image acquisition software sends serial data to the microcontroller to control the platform's movement, achieving a minimum precision of 1.25 μm (excluding inherent precision errors of the motor and guide rail). This precision is derived from the stepper motor's step angle (1.8°) and the lead of the 1204 ball screw (4 mm). Specifically, the linear displacement per step of the stepper motor is calculated by dividing the lead by the number of steps per revolution (200 steps), resulting in 4 mm / 200 = 0.02 mm (20 μm). By utilizing the 16 microstepping function of the A4988 driver module, each step is further divided into 16 microsteps, thereby enhancing the minimum displacement precision to 20 μm / 16 = 1.25 μm. In practical applications, the platform typically operates in an automated mode, following an S-shaped trajectory to ensure comprehensive coverage of the scanning area. Simultaneously, the host software saves the images captured by the image acquisition software sequentially to a predefined path.

Typically, the scanning area is defined as 1.0 cm $\times$ 1.0 cm. A standard-sized CR-39 detector sample (1.0 cm $\times$ 1.0 cm) is placed within this area for scanning, with only one sample scanned at a time. If the CR-39 detector is non-standard or larger in size, the scanning area can be flexibly adjusted to accommodate samples of different dimensions. During the scanning process of CR-39 detectors, individual image capture is used instead of video recording. This is because individual image capture provides higher resolution and image quality, enabling clearer detection of surface details on the detector. Additionally, static images are more suitable for subsequent processing tasks such as image stitching, track recognition, and counting, whereas video requires additional frame extraction steps, which not only increases processing complexity but may also lead to a decline in image quality. During this process, the system automatically acquires a total of 527 images through the automated control of the high-precision motion platform and the image acquisition software, arranged in a layout of 17 images horizontally and 31 images vertically. All images are positioned adjacently to cover the entire scanning area, although minor overlaps or missing regions may exist at the edges of the images. During the development phase, this issue was systematically evaluated through multiple experiments, and the results indicated that the impact of these overlaps or missing regions on the final outcome is negligible.

B. YOLOv8m-based alpha track counting module

YOLOv8 is a relatively advanced version in the YOLO series [17, 31, 32]. Taking into account the performance of existing equipment, an automatic track recognition and counting system was developed based on the open-source YOLOv8m deep learning framework, specifically designed for alpha-track analysis in CR-39 detectors. To ensure model performance and maximize the efficiency of manual annotation, this study selected four CR-39 materials with high track density as samples, each with dimensions of 9.7 mm $\times$ 9.7 mm. These detectors were etched in a 6.25M potassium hydroxide solution at 80°C for 12 hours. Research indicates that longer etching times result in clearer and larger track morphologies [33]. This treatment significantly enhanced the visibility of the tracks, providing high-quality data support for subsequent track annotation, image analysis, and model recognition. Additionally, the enlargement of tracks is particularly beneficial for the YOLOv8m object detection model, as larger track targets enable the model to capture feature information more accurately, thereby improving recognition precision and localization effectiveness. Using a high-resolution image acquisition system, images were captured for each sample in a layout of 17 images horizontally and 31 images vertically, resulting in 527 images per sample and a total of 2108 high-quality image data. These image data contain approximately 80000 alpha-track samples, which not only cover complete track morphologies but also include truncated tracks generated during the image acquisition process, ensuring the diversity and representativeness of the training data. This diverse dataset provides a solid foundation for model training and validation, enabling it to adapt to track recognition requirements in various scenarios.

During the data preprocessing stage, a rigorous manual an-

notation process was employed to precisely label the track samples: complete tracks were labeled as bubble, while truncated tracks were labeled as halfbubble. as shown in Fig. 2. This dual-label strategy not only enhances the accuracy of model training but also provides a reliable foundation for subsequent track classification and statistical analysis. It is worth noting that the shape of the tracks is closely related to parameters such as the incident angle and energy of the alpha-particles. For example, the incident angle of the alpha-particles affects the length and direction of the tracks, while the energy may influence the width and clarity of the tracks [34, 35]. Additionally, during the etching process, the tracks may become enlarged, potentially leading to overlapping of some tracks. However, these factors do not affect the annotation process. Regardless of the specific morphological variations of the tracks, the annotation process classifies them solely based on their completeness (complete or truncated), ensuring consistency in labeling and the effectiveness of model training. This design allows the system to adapt to track morphological variations under different experimental conditions while simplifying the complexity of the annotation process.

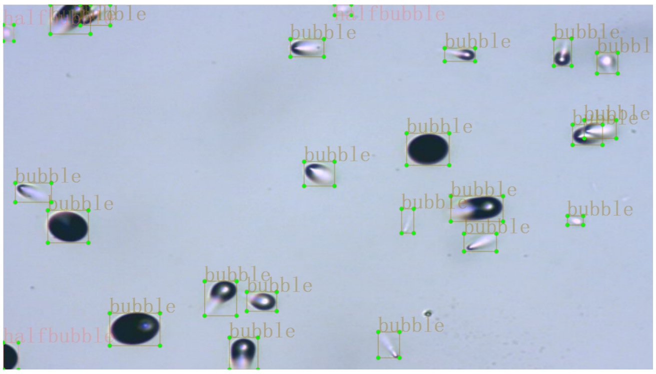

Fig. 2. Schematic diagram of different track samples.

Based on rigorously annotated training data, a YOLOv8m deep learning model was trained. As an open-source object detection framework, YOLOv8m employs an improved convolutional neural network (CNN) architecture, integrating a multi-scale feature pyramid network (FPN) and an adaptive feature fusion mechanism, significantly enhancing the accuracy and efficiency of track recognition. Specifically, FPN addresses the multi-scale object detection problem by constructing a top-down feature pyramid structure that combines high-level semantic information with low-level detailed information [36]. In track recognition tasks, FPN can simultaneously detect tracks of different scales by fusing high-resolution low-level features (capturing detailed information) and low-resolution high-level features (capturing semantic information), significantly improving the model's adaptability to complex scenarios.

As shown in Fig. 3, the backbone network (Backbone) of YOLOv8m consists of multiple convolutional layers (e.g., Conv0, Conv1, Conv3, Conv5, and Conv7) and C2f modules (e.g., C2f2, C2f4, C2f6, and C2f8). The convolutional layers extract local features from the input image through sliding windows, progressively capturing low-level features such as edges and textures, as well as more complex high-level features [37]. Then, these features are extracted and fused through the SPPF9 module, enhancing the model's ability to capture multi-scale features. Among them, SPPF (Spatial Pyramid Pooling - Fast) is an improved version of the SPP (Spatial Pyramid Pooling) technique in YOLOv8. The SPP technique generates fixed-length feature representations through multi-scale pooling operations, thereby addressing the issue of inconsistent input image sizes [38]. Building on SPP, SPPF optimizes the approach by replacing parallel pooling with sequential max-pooling operations, significantly reducing computational complexity while retaining the ability to extract multi-scale features [39, 40]. In the neck structure, the Feature Pyramid Network (FPN) upsamples low-resolution feature maps (e.g., Upsample10, Upsample13) to match the size of high-resolution feature maps [36]. Subsequently, concatenation operations (e.g., Concat11, Concat14, Concat17) are performed to connect feature maps from different levels along the channel dimension, achieving the fusion of multi-scale information and ultimately generating multi-scale feature maps (e.g., C2f12, C2f15, and C2f18). The detection head (Head) receives the fused feature maps from the neck and further extracts and fuses features through convolutional operations (e.g., Conv16, Conv19) and the C2f module (e.g., C2f21), completing classification and regression tasks and finally outputting the detection results. The C2f module enhances feature representation through cross-layer connections and feature fusion, significantly improving the model's detection performance for complex targets. The head structure processes these fused feature maps through a series of operations to generate the final predictions, including the target's category and location information, which are then output as detection results.

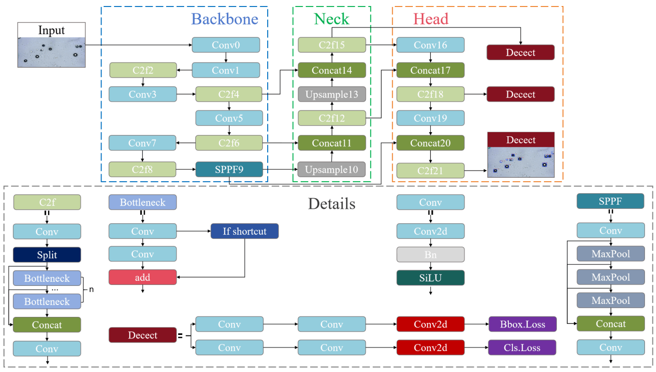

Fig. 3. YOLOv8 simplified network structure diagram.

The trained YOLOv8m model was integrated into a self-developed desktop software application. For this model, a processing strategy of recognizing before stitching 527 images (each with a resolution of 1280×720 pixels) was adopted, rather than stitching before recognizing, primarily for the following reasons: First, stitching 527 high-resolution images would result in an extremely large im-

age (approximately 17×31 arrangement, theoretically up to 21760×22320 pixels), which would significantly increase computational load and memory requirements, exceeding GPU processing capabilities and leading to reduced operational efficiency or even system crashes. Second, YOLOv8m achieves higher recognition accuracy on smaller-sized images, whereas overly large images may result in loss of detail or unstable recognition. Therefore, recognizing before stitching offers greater advantages in terms of computational efficiency, memory usage, and recognition accuracy.

The developed software enables real-time analysis of CR-39 detector images, accurately identifying and counting alpha tracks of various morphologies. Leveraging advanced image processing algorithms, the software can automatically distinguish between complete and truncated tracks and employs a weighted calculation method to precisely determine the total track count. It clearly marks the identified track positions, types, and sizes, with size information additionally generated in a separate text file. Furthermore, the software integrates an automatic image stitching function, seamlessly assembling the analyzed images into a complete CR-39 detector image. This feature facilitates visual verification of track counting and ensures traceability of experimental data.

C. Testing of the CR-39 detector automatic counting module

Ultimately, a total of 16 CR-39 detectors were selected for the final test set. These detectors had been utilized in various experimental environments, including measuring radon concentrations in granite, cement floors, and radon sources. Due to differences in experimental conditions, the measurement durations and radon concentration values of these detectors varied significantly, providing a rich experimental data foundation for the test set. This configuration not only ensured a wide distribution of track counts on the CR-39 detectors but also encompassed a variety of track types, providing a diverse sample set for model testing. The track counts on the detectors ranged from several thousand to tens of thousands, effectively simulating different scenarios that might be encountered in practical applications.

After the experiments were completed, the detectors were also etched in a 6.25M potassium hydroxide solution at 80°C for 12 hours to ensure the clarity of track morphologies. Following etching, the detectors underwent rigorous cleaning and wiping procedures to thoroughly remove residual chemical substances, thereby minimizing interference from impurities during the track recognition process. Ultimately, these processed detectors were used to evaluate the alpha-track automatic counting method developed in this study, verifying its robustness and accuracy under various experimental conditions.

The image acquisition system first performs comprehensive image capture of each CR-39 detector, ensuring that every area of the detector's surface is clearly and completely recorded. Subsequently, the developed automated counting system is activated, leveraging deep learning algorithms to process the acquired images. The system employs three different confidence thresholds—0.5, 0.6, and 0.7—to automatically identify and count tracks on all CR-39 detectors, while generating intuitive visual markers on the images. This process yields the model count value (V_m) for each detector, which represents the model's track identification results under specific confidence levels. After the automated counting is completed, researchers conduct a detailed inspection of the restored images, focusing on identifying potential omissions or misidentifications that may have occurred during the automated counting process. These errors are then corrected, resulting in the corrected count value (V_c). Although different researchers may obtain slightly varying results during the correction process, these differences are generally minor and have limited impact on the overall reliability of the statistical results. This value is considered to be closer to the true track count.

To clearly demonstrate the performance of the model, this study adopts the percentage error ($E_{\%}$) as the evaluation metric. The percentage error is calculated by comparing the difference between the model count value (V_m) and the corrected count value (V_c), with the specific formula shown in Eq. (1). This metric provides an intuitive reflection of the model's recognition accuracy at different confidence levels and serves as an important reference for optimizing the model.

$$E_{\%} = \left(\frac{V_m - V_c}{V_c}\right) \cdot 100\% \tag{1}$$

III. RESULTS AND DISCUSSION

The total time required for track counting on each CR-39 detector is approximately 16 minutes, with image acquisition taking 13 minutes, track recognition and counting requiring 1 minutes, and image restoration needing 2 minutes. It is worth noting that image acquisition and track recognition can be performed simultaneously. Additionally, the speed of track recognition is directly influenced by the performance of the computer's graphics card; the more powerful the graphics card, the faster the recognition speed. Compared to manual counting using a microscope, this method improves work efficiency by 2 to 10 times, achieving significant enhancements in analysis speed.

After the completion of testing and manual calibration, the model count values and corrected count values were calculated based on Eq. (1), and the corresponding percentage errors were derived. The results at confidence levels of 0.5, 0.6, and 0.7 are presented in Table 1, with the data sorted in ascending order based on the model count values. Notably, at the confidence level of 0.6, the false positive rate ($F_{\%}$) and missed detection rate ($M_{\%}$) were also included. The false positive rate ($F_{\%}$) is defined as the ratio of the number of over-identified tracks by the model to the calibrated value, which is a positive value reflecting the proportion of additional identifications by the model. The missed detection rate ($M_{\%}$) is defined as the ratio of the number of under-identified

Table 1. At confidence levels of 0.5, 0.6, and 0.7, the corrected count values (V_c), model count values (V_m), and error percentages ($E_{\%}$) for all CR-39 detectors are presented. Additionally, at a confidence level of 0.6, the false positive rate ($F_{\%}$), and missed detection rates($M_{\%}$) are included.

Detector number	V_c	At a confidence level of 0.5		At a confidence level of 0.6				At a confidence level of 0.7	
		V_m	$E_{\%}$	V_m	$E_{\%}$	$F_{\%}$	$M_{\%}$	V_m	$E_{\%}$
NO.1	1285	1331	3.58%	1297	0.93%	1.95%	-1.02%	1241	-3.42%
NO.2	1464	1510	3.14%	1476	0.82%	1.43%	-0.61%	1431	-2.25%
NO.3	1966	2039	3.71%	1960	-0.31%	1.22%	-1.53%	1881	-4.32%
NO.4	3645	3744	2.71%	3629	-0.44%	0.66%	-1.10%	3503	-3.90%
NO.5	3925	4004	2.01%	3909	-0.41%	0.36%	-0.77%	3790	-3.44%
NO.6	5086	5230	2.83%	5093	0.14%	0.41%	-0.27%	4961	-2.46%
NO.7	6619	6773	2.32%	6646	0.41%	0.83%	-0.42%	6496	-1.86%
NO.8	7270	7480	2.89%	7250	-0.28%	0.52%	-0.80%	6985	-3.92%
NO.9	9606	9752	1.52%	9512	-0.98%	0.32%	-1.30%	9193	-4.30%
NO.10	11954	12247	2.45%	11927	-0.23%	0.80%	-1.03%	11548	-3.40%
NO.11	12489	12760	2.17%	12368	-0.97%	1.03%	-2.00%	11850	-5.12%
NO.12	12451	12733	2.27%	12404	-0.38%	0.83%	-1.21%	12030	-3.38%
NO.13	13013	13299	2.20%	12960	-0.41%	0.70%	-1.11%	12486	-4.05%
NO.14	15728	16078	2.23%	15643	0.54%	0.64%	-1.18%	15057	-4.27%
NO.15	18342	18662	1.74%	18272	-0.38%	1.32%	-1.70%	17762	-3.16%
NO.16	18944	19331	2.04%	18806	-0.73%	1.17%	-1.90%	18105	-4.43%

tracks by the model to the calibrated value, which is a negative value reflecting the proportion of actual tracks that the model failed to identify.

Data analysis reveals that there are discrepancies between the model count values and the calibrated count values for the selected 16 CR-39 detectors at different confidence levels. In the model trained with 80000 alpha-track samples for this exercise, when the confidence level is set to 0.5, the prediction error is typically maintained at around 2.5%, and the model count values often exceed the calibrated count values. This may be because, at lower confidence levels, some uncertain targets are retained, leading to an overestimation of the total number of tracks. When the confidence level is increased to 0.6, the false positive rate and the missed detection rate partially offset each other, thereby reducing the overall error and bringing the model count values closer to the calibrated count values. At a confidence level of 0.7, the model count values are generally lower than the calibrated count values, possibly because the model filters out predictions it is less confident about. Overall, these discrepancies may be attributed to the limited number of training samples, resulting in fluctuations in the model's performance across different confidence levels.

To visually analyze and apply these data, linear fitting was performed using Origin software, with the specific results shown in Fig. 4. The fitting results clearly demonstrate a linear relationship between the data. When the confidence levels are 0.5, 0.6, and 0.7, the R-squared values for the fitting curves of the model count values (V_m) and the corrected count values (V_c) are 0.99997, 0.99997, and 0.99981, respectively. This indicates a strong correlation between the predicted model values and the corrected count values. Notably, when the confidence level is 0.6, the slope of the fitting curve is closest to 1, indicating that the linear relationship between the model count values and the corrected count values is most ideal at this confidence level, with the smallest deviation between predicted and actual values.

The analysis results indicate that variations in track count have a negligible impact on the predictive performance of the model. Despite the limited sample size of CR-39 detectors tested, the model demonstrates excellent predictive consistency across different track density conditions. This suggests that the model exhibits significant robustness within a certain range of track density variations. However, to further validate the reliability of the model and comprehensively assess its applicability under complex conditions, subsequent research should systematically expand testing based on larger datasets and a broader range of track densities.

Meanwhile, a preliminary statistical analysis of the size of complete tracks on these 16 CR-39 detectors was conducted based on the recognition results with a confidence threshold of 0.6. During the statistical process, truncated tracks were excluded because their length and width information is incomplete and cannot accurately reflect their true dimensions. Additionally, problematic tracks identified during the recognition process, such as those with abnormal morphology or difficult to distinguish from impurities, accounted for a very small proportion, having a negligible impact on the overall statistical results.

To visually demonstrate the distribution patterns of track sizes, heatmap analysis was employed to systematically study the width and height data of tracks from all detectors. It should be noted that truncated tracks were excluded from the statistical analysis due to incomplete size information. Under the current etching conditions and with a recognition confi-

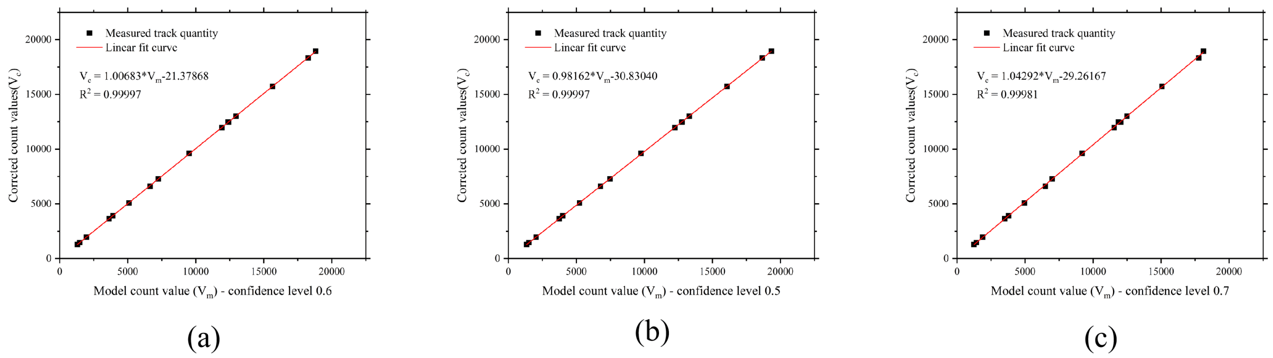

Fig. 4. The correlation between the model count value and the corrected count value: (a) at a confidence level of 0.5, (b) at a confidence level of 0.6, and (c) at a confidence level of 0.7.

dence threshold of 0.6, the detectors can be categorized into three groups based on track size distribution characteristics: The first group includes detectors NO. 3, 4, 5, 8, 10, 11, 13, 14, and 16, where track sizes are predominantly concentrated in the range of 12-22 μm (width) $\times$ 12-22 μm (length), with NO. 16 being the most representative, as shown in Fig. 5(a). The second group comprises detectors NO. 1, 2, 7, 9, 12, and 15, which exhibit significant distributions in both the 12-22 μm (width) $\times$ 12-22 μm (length) and 30-40 μm (width) $\times$ 30-40 μm (length) ranges, with NO. 9 serving as the representative, as illustrated in Fig. 5(b). The third group is detector NO. 6, where track sizes are mainly distributed in the range of 30-40 μm (width) $\times$ 30-40 μm (length), as depicted in Fig. 5(c). To further comprehensively characterize the overall distribution features of track sizes, the complete track data from all 16 detectors were integrated, and a comprehensive heatmap was generated, as shown in Fig. 5(d). The analysis results reveal a significant non-uniformity in track size distribution: small-sized tracks in the range of 12-22 μm (width) $\times$ 12-22 μm (length) dominate, while medium-to-large tracks in the range of 30-40 μm (width) $\times$ 30-40 μm (length) are relatively fewer in number. It is noteworthy that although the exclusion of truncated tracks has somewhat affected the statistical count of medium-to-large tracks (as larger tracks are more prone to truncation due to their size), this does not alter the dominant distribution pattern of small-sized tracks in the overall sample. This phenomenon may be closely related to multiple factors, including track formation mechanisms, detector surface characteristics, and etching conditions.

To identify the sources of recognition errors, several key issues during the preparation and execution stages of detector acquisition have been identified, which may affect the experimental results. Firstly, adjusting the microscope's focus is a critical step that must be precisely completed before image acquisition to ensure that the microscope maintains accurate focus during the movement of the stage. If the focus is not properly adjusted, the tracks in the image may become blurry, which not only affects the recognition accuracy of the YOLOv8m model but may also result in some tracks being undetectable. Secondly, vibration is another significant factor that cannot be overlooked. Even slight vibrations, such

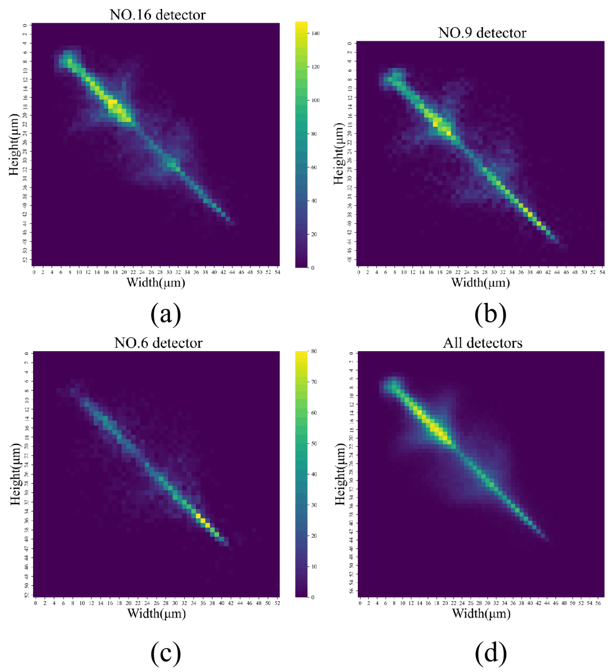

Fig. 5. Heatmap of track size distribution on CR-39 detectors: (a) NO.16 detector, (b) NO.9 detector, (c) NO.6 detector, (d) All detectors.

as mechanical vibrations in the experimental environment or instability of the operating platform, can cause image blurring, thereby interfering with the model's accurate recognition. Additionally, variations in ambient lighting can also negatively impact imaging quality. However, although these issues may introduce some interference to the experimental results, they are considered minor sources of error and can be resolved by optimizing hardware equipment or improving experimental conditions. For example, using a higher-precision microscope focusing system, enhancing equipment stability, or implementing vibration isolation measures in the experimental environment can effectively reduce these errors. At the same time, controlling ambient lighting and optimizing

image acquisition parameters can further improve imaging quality.

During the calibration and analysis of tracks in CR-39 detectors, several issues requiring attention have been identified. Firstly, the presence of impurities—such as fingerprints, dust, or inherent defects introduced during the manufacturing process—particularly those with shapes highly similar to tracks, may interfere with the analysis results. Secondly, during the image acquisition process, due to the resolution limitations of the equipment, tracks located at the edges of the image may be split into multiple parts, leading to the problem of over-counting tracks. Additionally, a single track may sometimes be divided into two segments, which the model might misinterpret as two independent tracks or identify as one complete track and one truncated track. Another scenario is that two tracks may overlap due to the etching process, causing the model to recognize them as a single track. However, the occurrence of these situations is extremely rare and has a negligible impact on the final results.

To improve the overall recognition accuracy, during the data collection phase, higher-resolution electronic eyepieces can be used for image capture, allowing a larger field of view to be covered in a single image. This reduces the number of images required and minimizes the probability of tracks being truncated. Secondly, during the model training phase, increasing the quantity and diversity of training samples (covering different etching conditions and impurity types) can significantly enhance the model's ability to recognize real tracks, reducing false positives and missed detections. Additionally, in terms of model selection, exploring other advanced deep learning models is also an effective strategy. Although other object detection algorithms (such as Single Shot MultiBox Detector and Mask R-CNN) may theoretically offer faster inference speeds, their specific performance requires further experimental validation, and their training costs and hardware requirements may also be higher. Therefore, a balance between performance and cost must be considered in practical applications.

IV. CONCLUSION

This study delves into the potential application of YOLO series algorithms in alpha track counting on CR-39 detectors, providing an efficient tool for radon measurement based on CR-39 detectors while eliminating the cumbersome process of traditional manual counting. The research team developed a CR-39 image acquisition system based on a microcontroller, optical microscope, and PY-QT modules, and trained a YOLOv8m-based image recognition model using over 80000 alpha track samples. This model not only enables automatic detection and counting of alpha tracks but also supports the reconstruction of CR-39 detector images, significantly improving the efficiency and accuracy of data processing.Tests conducted on 16 CR-39 detectors with different track densities revealed that the model's automatic recognition performance varies significantly at different confidence levels. Among the three tested confidence levels (0.5, 0.6, and 0.7), the model count values were closest to the calibrated count values at a confidence level of 0.6, demonstrating optimal predictive consistency. Linear regression analysis further confirmed a high correlation ($R^2 > 0.99$) between the predicted and corrected count values, validating the model's reliability. Meanwhile, the track sizes on these detectors are primarily concentrated in the range of 12-22 μm (width) $\times$ 12-22 μm (length), with fewer tracks in the 30-40 μm (width) $\times$ 30-40 μm (length) range.

To improve the accuracy of track recognition, it is necessary to address certain issues during the acquisition process, such as ensuring precise microscope focusing, minimizing vibrations in the experimental environment, and controlling lighting conditions. By adopting higher-resolution electronic eyepieces, increasing the diversity of training samples, and exploring advanced deep learning models, the recognition performance of the model can be effectively enhanced. This will provide more reliable technical support for the automated analysis of alpha tracks in CR-39 detectors.

---

[1] M. Ćujić, L. Janković Mandić, J. Petrović et al., Radon-222: environmental behavior and impact to (human and non-human) biota. Int. J. Biometeorol. **65**, 69–83 (2021). doi: 10.1007/s00484-020-01860-w

[2] J.K. Kang, S. Seo, Y.W. Jin, Health effects of radon exposure. Yonsei Med. J. **60**, 597–603 (2019). doi: 10.1108/ss.2009.11027eab.001

[3] J.Y. Yoon, J.D. Lee, S.W. Joo et al., Indoor radon exposure and lung cancer: a review of ecological studies. Ann. Occup. Environ. Med. **28**, 1–9 (2016). doi: 10.1186/s40557-016-0098-z

[4] J.W.N. Tuyn, Solid state nuclear track detectors in reactor physics experiments. Nucl. Appl. **3**, 372–374 (1967). doi: 10.13182/NT67-A27860

[5] Y. Cheng, J. Lin, B. Zhang et al., Measurement of fast neutron fluences by the nuclear track technique. Nucl. Instrum. Methods Phys. Res. B **52**, 68–71 (1990). doi: 10.1016/0168-583X(90)90603-R

[6] D. Nikezic, K.N. Yu, Computer program TRACK_TEST for calculating parameters and plotting profiles for etch pits in nuclear track materials. Comput. Phys. Commun. **174**, 160–165 (2006). doi: 10.1016/j.cpc.2005.09.011

[7] M.A. Rana, CR-39 nuclear track detector: An experimental guide. Nucl. Instrum. Methods Phys. Res. A **910**, 121–126 (2018). doi: 10.1016/j.nima.2018.08.077

[8] Z. Fan, J. Shan, F. Lin et al., Developing a radon monitor for simultaneous measurement of Rn-222 and Rn-220 with less influence of humidity based on electrostatic collection and CR-39 detector. Nucl. Instrum. Methods Phys. Res. A **1052**, 168285 (2023). doi: 10.1016/j.nima.2023.168285

[9] Y. Zhang, L.X. Liu, H.W. Wang et al., Primary yields of protons measured using CR-39 in laser-induced deuteron–deuteron

fusion reactions. Nucl. Sci. Tech. **31**, 62 (2020). doi: 10.1007/s41365-020-00769-8

[10] S. Yang, J. Zhao, W. Zhuo et al., Measurement of therapeutic 12C beam in a water phantom using CR-39. J. Radiol. Prot. **41**, 279 (2021). doi: 10.1088/1361-6498/ABD88C

[11] Z. Fan, J. Shan, F. Lin et al., Developing a radon monitor for simultaneous measurement of Rn-222 and Rn-220 with less influence of humidity based on electrostatic collection and CR-39 detector. Nucl. Instrum. Methods Phys. Res. A **1052**, 168285 (2023). doi: 10.1016/j.nima.2023.168285

[12] J.H. Adams Jr, Automated track measurements in CR-39. Nucl. Tracks **4**, 67–76 (1980). doi: 10.1016/0191-278X(80)90016-5

[13] G. Bátor, A. Csordás, D. Horvath et al., A comparison of a track shape analysis-based automated slide scanner system with traditional methods. J. Radioanal. Nucl. Chem. **306**, 333–339 (2015). doi: 10.1007/s10967-015-4013-9

[14] K.M. Abumurad, A.M. Ismail, H. Abu-Safia, A photometry method for measuring tracks density on SSNTDs. Radiat. Meas. **40**, 303–306 (2005). doi: 10.1016/j.radmeas.2005.03.020

[15] H. Alameri, Y. Abou-Ali, M.H. Obeid et al., Estimation of alpha exposure on CR-39 detector using a UV-VIS spectrophotometer. Appl. Radiat. Isot. **209**, 111331 (2024). doi: 10.1016/j.apradiso.2024.111331

[16] E. Hulber, Overview of PADC nuclear track readers. Recent trends and solutions. Radiat. Meas. **44**, 821–825 (2009). doi: 10.1016/j.radmeas.2009.10.097

[17] J. Redmon et al., in *Proceedings of the IEEE Conference on Computer Vision and Pattern Recognition*, ed. by IEEE. IEEE Conference on Computer Vision and Pattern Recognition, Las Vegas, June 2016. (IEEE, 2016), p. 779–788.

[18] X. Zhu, D. Li, Y. Zheng et al., A YOLO-Based Model for Detecting Stored-Grain Insects on Surface of Grain Bulks. Insects **16**, 210 (2025). doi: 10.3390/insects16020210

[19] T. Li, L. Zhang, J. Lin, Precision agriculture with YOLO-Leaf: advanced methods for detecting apple leaf diseases. Front. Plant Sci. **15**, 1452502 (2024). doi: 10.3389/fpls.2024.1452502

[20] X.L. Li, F.Y. Wang, Y. Guo et al., Improved YOLO v5s-based detection method for external defects in potato. Front. Plant Sci. **16**, 1527508 (2025). doi: 10.3389/FPLS.2025.1527508

[21] Y. Meng, J. Zhan, K. Li et al., A rapid and precise algorithm for maize leaf disease detection based on YOLO MSM. Sci. Rep. **15**, 6016 (2025). doi: 10.1038/s41598-025-88399-1

[22] S.Y. Lee, P.M. Patil, G.J. Kim et al., Improved tomato leaf disease recognition based on the YOLOv5m with various soft attention module combinations. Agriculture **14**, 1472 (2024). doi: 10.3390/agriculture14091472

[23] R. Murendeni, A. Mwanza, C.I. Obagbuwa, Using a YOLO Deep Learning Algorithm to Improve the Accuracy of 3D Object Detection by Autonomous Vehicles. World Electr. Veh. J. **16**, 9 (2024). doi: 10.3390/wevj16010009

[24] Y. Zhang, X. Hou, X. Hou, Combining Self-Supervised Learning and Yolo v4 Network for Construction Vehicle Detection. Mob. Inf. Syst. **2022**, 9056415 (2022). doi: 10.1155/2022/9056415

[25] C. Jiang, H. Ren, X. Ye et al., Object detection from UAV thermal infrared images and videos using YOLO models. Int. J. Appl. Earth Obs. Geoinf. **112**, 102912 (2022). doi: 10.1016/j.jag.2022.102912

[26] Z. Zhang, X. Xie, Q. Guo et al., Improved YOLOv7-Tiny for object detection based on UAV aerial images. Electronics **13**, 2969 (2024). doi: 10.3390/electronics13152969

[27] S. Wang, Y. Liu, X. Wang et al., An improved YOLO algorithm for UAV detection in formation flight. Signal Image Video Process. **19**, 1–8 (2025). doi: 10.1007/s11760-024-03660-w

[28] S. Jiao, F. Xu, H. Guo, Side-Scan Sonar Image Detection of Shipwrecks Based on CSC-YOLO Algorithm. Comput. Mater. Contin. **82**, 2 (2025). doi: 10.32604/CMC.2024.057192

[29] X. Gao, L. Zhang, X. Chen et al., GCT-YOLOv5: a lightweight and efficient object detection model of real-time side-scan sonar image. Signal Image Video Process. **18**, 565–574 (2024). doi: 10.1007/s11760-024-03174-5

[30] S. Fu, H. Pan, J. Huang et al., AGD-YOLO: a forward-looking sonar target detection method with attention-guided denoising convolutional neural network. Aerosp. Syst. (2025): 1–16. doi: 10.1007/s42401-025-00352-2

[31] Q. Zhou, Z. Wang, Y. Zhong et al., Efficient Optimized YOLOv8 Model with Extended Vision. Sensors **24**, 6506 (2024). doi: 10.3390/s24206506

[32] M. Sportelli, O.E. Apolo-Apolo, M. Fontanelli et al., Evaluation of YOLO object detectors for weed detection in different turfgrass scenarios. Appl. Sci. **13**, 8502 (2023). doi: 10.3390/app13148502

[33] S. Kodaira, M. Janik, Spectroscopic analysis of alpha particles from radioactive nuclides with CR-39 plastic nuclear track detectors. Radiat. Prot. Dosim. **200**, 1686–1691 (2024). doi: 10.1093/rpd/ncae068

[34] Y.L. Law, D. Nikezic, K.N. Yu, Optical appearance of alpha-particle tracks in CR-39 SSNTDs. Radiat. Meas. **43**, S128–S131 (2008). doi: 10.1016/j.radmeas.2008.03.030

[35] A.K. Mheemeed, A.K. Hussein, R.B. Alkhayat, Characterization of alpha-particle tracks in cellulose nitrate LR-115 detectors at various incident energies and angles. Appl. Radiat. Isot. **79**, 48–55 (2013). doi: 10.1016/j.apradiso.2013.04.020

[36] T.Y. Lin et al., in *Proceedings of the IEEE Conference on Computer Vision and Pattern Recognition*, ed. by IEEE. IEEE Conference on Computer Vision and Pattern Recognition, Honolulu, July 2017. (IEEE, 2017), p. 2117–2125.

[37] Y. LeCun, Y. Bengio, G. Hinton, Deep learning. Nature **521**, 436–444 (2015). doi: 10.1038/nature14539

[38] K. He, X. Zhang, S. Ren et al., Spatial pyramid pooling in deep convolutional networks for visual recognition. IEEE Trans. Pattern Anal. Mach. Intell. **37**, 1904–1916 (2015). doi: 10.1007/978-3-319-10578-9_23

[39] J. Huang, C. Fang, X. Zheng et al., YOLOv8-UC: An Improved YOLOv8-Based Underwater Object Detection Algorithm. IEEE Access (2024). doi: 10.1109/ACCESS.2024.3496925

[40] H. Wang, K. Ma, J. Yue et al., Small-Target Detection Based on Improved YOLOv8 for Infrared Imagery. Electronics **14**, 947 (2025). doi: 10.3390/ELECTRONICS14050947